

A New Integration Method for an Electric Vehicle Wireless Charging System Using *LCC* Compensation Topology: Analysis and Design

Tianze Kan, *Student Member, IEEE*, Trong-Duy Nguyen, Jeff C. White, Rajesh K. Malhan, and Chunting Chris Mi, *Fellow, IEEE*

Abstract—There is a need for charging electric vehicles (EVs) wirelessly since it provides a more convenient, reliable, and safer charging option for EV customers. A wireless charging system using a double-sided *LCC* compensation topology is proven to be highly efficient; however, the large volume induced by the compensation coils is a drawback. In order to make the system more compact, this paper proposes a new method to integrate the compensated coil into the main coil structure. With the proposed method, not only is the system more compact, but also the extra coupling effects resulting from the integration are either eliminated or minimized to a negligible level. Three-dimensional finite-element analysis tool ANSYS MAXWELL is employed to optimize the integrated coils, and detailed design procedures on improving system efficiency are also given in this paper. The wireless charging system with the proposed integration method is able to transfer 3.0 kW with 95.5% efficiency (overall dc to dc) at an air gap of 150 mm.

Index Terms—Coil design, electric vehicle (EV) charging, wireless power transfer (WPT).

I. INTRODUCTION

FOR centuries, engineers are seeking to transfer power wirelessly [1]–[5]. Nowadays, wireless power transfer (WPT) technology is widely used in powering biomedical implants, tooth brush, cell phones, laptops, and even plugin hybrid electric vehicles (PHEVs) and electric vehicles (EVs). The power level ranges from several milliwatts to tens of kilowatts [6]–[16], [18]–[21]. The inductive-based wireless charging for PHEVs and EVs is highly acknowledged since it provides a more convenient, reliable, and safer charging option compared to conductive charging. The research in this field is of a great variety, such as coil design, power electronics converters and control method, compensation topologies, foreign object detection, and safety

Manuscript received January 13, 2016; revised March 7, 2016; accepted March 28, 2016. Date of publication April 7, 2016; date of current version November 11, 2016. This work was supported in part by the US Department of Energy Graduate Automotive Technology Education Grant, the US-China Clean Energy Research Center–Clean Vehicle Consortium, DENSO International, and San Diego State University. Recommended for publication by Associate Editor O. Lucia.

T. Kan is with Department of Electrical and Computer Engineering, San Diego State University, San Diego, CA 92182 USA, and is also with the Department of Electrical and Computer Engineering, University of California at San Diego, La Jolla, CA 92093 USA (e-mail: bigtreehust@gmail.com).

T.-D. Nguyen, J. C. White, and R. K. Malhan are with DENSO International America, Inc., Southfield, MI 48033 USA (e-mail: ntrduy@gmail.com; jeff_c_white@denso-diam.com; rajesh_k_malhan@denso-diam.com).

C. C. Mi is with Department of Electrical and Computer Engineering, San Diego State University, San Diego, CA 92182 USA (e-mail: cmi@sdsu.edu).

Color versions of one or more of the figures in this paper are available online at <http://ieeexplore.ieee.org>.

Digital Object Identifier 10.1109/TPEL.2016.2552060

issues. Among them, coil design and compensation topologies are two main research areas.

Coils are the essence of an inductive-based wireless charging system. They determine the power transfer capability and transfer efficiency. One important property of the coils is the geometry as it closely relates to the coupling coefficient of the coil structure and the quality factor of each coil. Budhia *et al.* [8] give the design and optimization procedures for circular coils and demonstrates a 2 kW 700-mm diameter pad. Takashi *et al.* [9] present a flux-pipe coil structure and claims that a charging system can transfer 3.0 kW power with 90% efficiency at an air gap of 200 mm. However, the flux-pipe coil conducts double-sided flux paths and one of the flux paths is wasted. In order to solve this problem, a bipolar coil structure is developed in [10]. The bipolar coil structure offers high efficiency and good misalignment tolerance. An 8 kW wireless charging system is built and tested in [11]. With the optimized bipolar coil structure, the charger can transfer power with 95.66% efficiency when fully aligned and 95.39% efficiency with a 300 mm horizontal misalignment. More recent research on coil design can be found in [22]. The researchers embed a coplanar coil into the primary coil system to improve the overall coupling of the system, which increases the efficiency with the SS compensation topology.

Compensation topology is another important aspect in a wireless charging system as it increases the power transfer ability, minimizes the VA rating of the power source, and helps achieve soft switching of the power electronics devices [23]. There are four basic compensation topologies: SS, SP, PS, and PP where the letters “P” and “S” stand for the way how the resonant capacitor is connected to the coil, i.e., “P” represents parallel connection and “S” represents series connection. More advantageous compensation topologies are put forward in [12] and [13]. The double-sided *LCC* compensation topology is outstanding since not only is its resonant frequency independent of coupling coefficient and load condition, but also it is highly efficient [13]. However, one drawback of the double-sided *LCC* compensation topology is its large volume due to the compensated coils.

To overcome the volume limitation, Li *et al.* [14] first put forward the idea of integrating the compensated coil into the main coil system. The authors integrate a bipolar compensated coil into a bipolar main coil system. As it is shown in Fig. 1, five extra coupling effects appear after the integration and the coupling effect of the two coils at the same side of the wireless charging system are studied. A 6 kW wireless charging system with 95.3% efficiency was designed and tested in [14]. Further

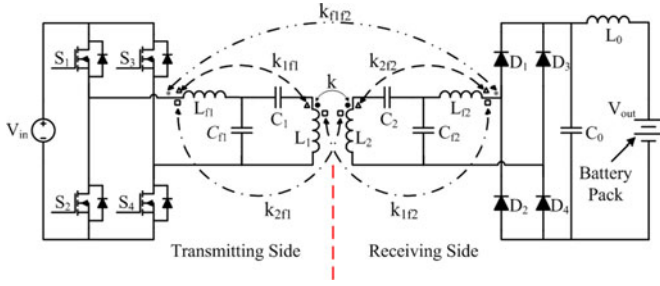


Fig. 1. Double-sided LCC compensation topology with compensated coils' integration.

detailed analysis on both the coupling effect of the same-side coils and the coupling effect of the cross-side coils can be found in [15] and [16]. The study in [14]–[16] successfully make the system more compact and highly efficient; however, the method of integration complicates the design of a wireless charging system using double-sided LCC compensation topologies.

In order to simplify the design and analysis while keeping the advantages of compactness and high efficiency, this paper proposes a new integration method for a wireless charging system using LCC compensation topology. In this method, the five extra coupling effects are either eliminated or minimized to a neglected level, which greatly simplifies the design and analysis. Additionally, a new method of improving system efficiency is given. Consequently, the system keeps outstanding performance and is able to deliver 3.0 kW power with 95.5% dc–dc efficiency at an air gap of 150 mm.

II. ANALYSIS

The double-sided LCC compensation topology is proven to be highly efficient for WPT applications in EVs and plug-in EVs [13]–[16]. Fig. 1 shows a wireless charging system using the double-sided LCC compensation topology. The dc input is transformed to a high frequency ac power by a full-bridge inverter, which is formed by MOSFET switches S_1 – S_4 . On the transmitting side, also known as the primary side, L_{f1} , C_{f1} , C_1 , and L_1 constitute the primary resonant tank, which is tuned to have a resonant frequency the same with the switching frequency of the full-bridge inverter. The high frequency ac power resonates in the primary resonant tank. On the receiving side, which is also called the secondary side, L_{f2} , C_{f2} , C_2 , and L_2 make up the secondary resonant tank. In order to receive power from the transmitting side, the secondary resonant tank also has the same resonant frequency. Since there is no wire connection between the transmitting side and the receiving side, the high frequency ac power is transmitted wirelessly through the main coupling between the main coils L_1 and L_2 . Afterwards, it is converted back to dc by the rectifier consist of four diodes D_1 – D_4 . After being further filtered by the CL-filter, the power is qualified to charge the battery packs.

As can be seen from Fig. 1, a double-sided LCC compensation topology involves four magnetic components: L_{f1} , L_1 , L_2 , and L_{f2} where L_1 and L_2 are the main coils while L_{f1} and L_{f2} are the compensated coils. L_{f1} and L_{f2} are air-core inductors; however, the large dimension of air-core inductors is not

practical in reality. In order to make the system more compact, we propose to integrate the compensated coils into the main coil system. Once they are integrated, extra couplings appear. As shown in Fig. 1, six couplings exist and the coupling coefficients are chosen to represent their coupling effects, where “ k ” stands for the coupling coefficient between the main coils L_1 and L_2 while “ k_{f1f2} ” represents the coupling coefficient between compensated coils L_{f1} and L_{f2} ; “ k_{1f1} ” is the coupling coefficient between L_1 and L_{f1} and similarly, “ k_{2f2} ” is the coupling coefficient between L_2 and L_{f2} , “ k_{1f1} ” and “ k_{2f2} ” refer to the same-side coupling coefficients; “ k_{1f2} ” and “ k_{2f1} ” are the coupling coefficient between L_1 and L_{f2} , the coupling coefficient between L_2 and L_{f1} , respectively, “ k_{1f2} ” and “ k_{2f1} ” are also known as cross-side coupling coefficients. Moreover, in Fig. 1, the main coupling coefficient k is represented by a solid line while the other five is in dashed or dash-dot lines. WPT relies on the main coupling to transmit power wirelessly between the transmitting side and the receiving side; therefore, the main coupling between L_1 and L_2 is of great significance and the other five couplings are redundant. The goal is to maximize the main coupling and eliminate the five extra couplings or minimize their coupling effects to a negligible level.

Fig. 2 presents the proposed integrated coil structure. Bipolar coils are selected as the main coils L_1 and L_2 because of the outstanding performance and good misalignment tolerance [11]. Due to the onboard space limitation, the size of the secondary side is smaller than that of the primary side. Unipolar coils are chosen for compensated coils L_{f1} and L_{f2} . Since both the primary side and the secondary side have similar coil structures, analysis will be first focused on one side. On the primary side, the bipolar coil L_1 performs as a magnetic dipole and the magnetic flux excited by L_1 passes through the compensated coil L_{f1} . The amount of the magnetic flux can be expressed as ψ_{1f1}

$$\psi_{1f1} = \iint \vec{B}_1 \cdot d\vec{S}_{f1} \quad (1)$$

where “ B_1 ” stands for the magnetic flux density and “ S_{f1} ” represents the area of the primary compensated coil L_{f1} . The compensated coil is placed in the center of the coil structure in a different layer. As a main characteristic of a magnetic dipole, the magnetic flux it excites is symmetrical in space; therefore, the amount of the magnetic flux flows into the compensated coil equals to that flows out of it. As a result, the net magnetic flux passing through L_{f1} is zero. Since ψ_{1f1} is zero, the coupling coefficient is zero so the coupling effect is eliminated

$$k_{1f1} = \sqrt{\frac{\psi_{1f1}\psi_{f11}}{\psi_{11}\psi_{1f1}}} = 0 \quad (2)$$

where ψ_{f11} is the amount of magnetic flux excited by L_{f1} passes through L_1 , ψ_{11} and ψ_{f1f1} represent the amounts of their self-magnetic flux. Similarly, the net amount of magnetic flux which is excited by L_2 and passes through L_{f2} is zero so the coupling coefficient k_{2f2} is zero. Moreover, the net amount of magnetic flux which is excited by L_1 and passes through L_{f2} is zero and the net amount of magnetic flux which is excited by L_2 and passes through L_{f1} is also zero. The coupling coefficients of cross-side coils k_{1f2} and k_{2f1} are both zero. When fully

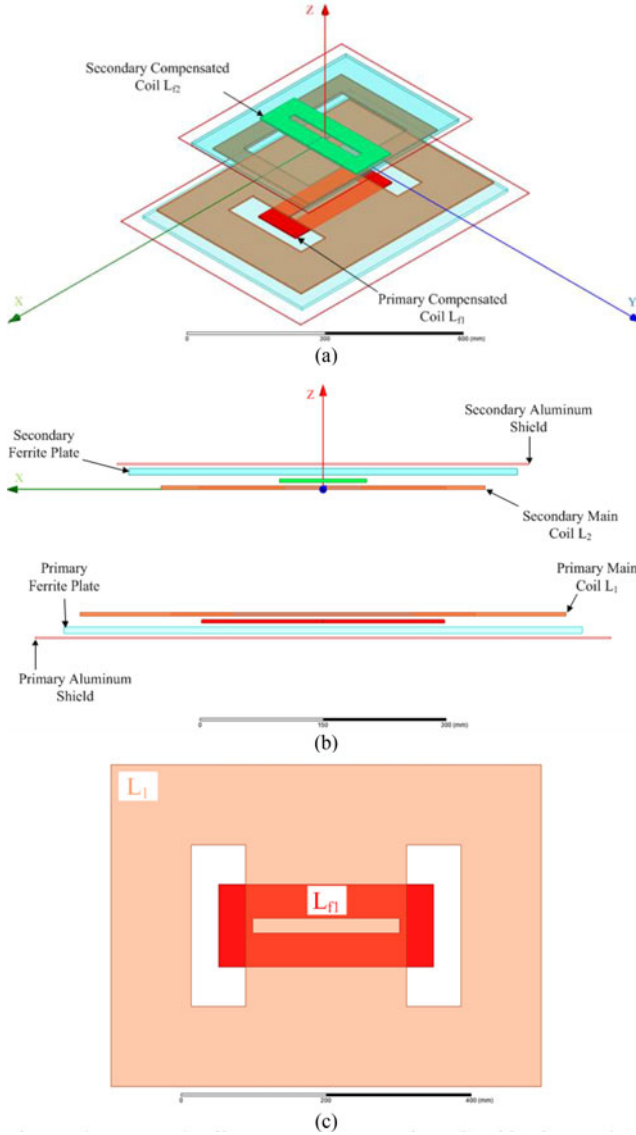


Fig. 2. Proposed coil structures: (a) overview, (b) side view, and (c) primary coils.

aligned, the four coupling effects are eliminated. Furthermore, when misalignment between the primary side coil structure and the secondary side coil structure occurs, the four inductance values almost do not change. Since the relative positions of the same-side coils are fixed, the same-side coupling coefficients k_{1f1} and k_{2f2} are still zero. Though the relative positions of the cross-side coils change, the cross-side coupling effects can be neglected. It is because the compensated coil inductance values are multiple times smaller than the main coil inductance values and the air gap between the main coil and compensated coil is considered large when compared with coil dimensions. Additionally, the coupling coefficient k_{f1f2} can be minimized to a negligible level by 3-D finite-element analysis (FEA) tool when fully aligned, which will be discussed in next section. When misalignment occurs, k_{f1f2} will be further decreased because the relative positions of the compensated coils change.

The five extra coupling coefficients are either eliminated or minimized to a negligible level; the following analysis will be

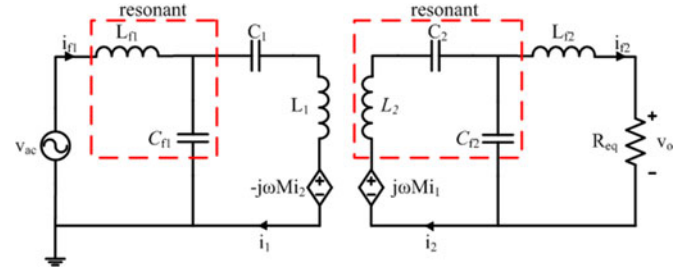


Fig. 3. Resonant circuits with double-sided LCC compensation topology.

only focused on the main coupling coefficient k between L_1 and L_2 . The input dc voltage is converted to a square wave voltage of a designed frequency and enters into the primary resonant tank, where the voltage and its resulting current resonate at the resonant frequency. The resonant tank also serves as a filter and almost all high-frequency components are filtered out. Therefore, first harmonic analysis is applied in analyzing the double-sided LCC compensation topology. Here, “ v_{ac} ” in (3) refers to the fundamental component of the square wave voltage. Furthermore, the battery pack is considered to be a constant voltage source when designing the circuit. Since the output power is constant, the battery pack is modeled as a load resistor R_L in (4). The root mean square (rms) output current of the double-sided LCC compensation topology is constant once the input voltage is fixed. Therefore, the load resistor can be converted equivalently to R_{eq} at the input side of the rectifier [17]

$$v_{ac} = \frac{2\sqrt{2}}{\pi} V_{in} \angle 0^\circ \quad (3)$$

$$R_L = \frac{V_{out}^2}{P_{out}} \quad (4)$$

$$R_{eq} = \frac{8}{\pi^2} R_L = \frac{8}{\pi^2} \cdot \frac{V_{out}^2}{P_{out}} \quad (5)$$

In Fig. 3, L_{f1} resonates with C_{f1} and as a result, i_1 is constant once v_{ac} is fixed. “ $j\omega Mi_1$ ” can be treated as a constant voltage source for the secondary resonant tank. C_2 is chosen to compensate L_2 such that the series impedance of L_2 and C_2 is equal to that of L_{f2} . L_2 and C_2 resonate with C_{f2} . Therefore, the output current i_{f2} is also constant, which is desired for battery charging

$$\omega L_{f1} - \frac{1}{\omega C_{f1}} = 0 \quad (6)$$

$$\omega L_2 - \frac{1}{\omega C_2} - \frac{1}{\omega C_{f2}} = 0 \quad (7)$$

$$i_1 = \frac{v_{ac}}{j\omega L_{f1}} = \frac{2\sqrt{2}}{\pi} \cdot \frac{V_{in}}{\omega L_{f1}} \angle -90^\circ \quad (8)$$

$$i_{f2} = \frac{k\sqrt{L_1 L_2} v_{ac}}{j\omega L_{f1} L_{f2}} = \frac{2\sqrt{2}}{\pi} \cdot \frac{k\sqrt{L_1 L_2} V_{in}}{\omega L_{f1} L_{f2}} \angle -90^\circ \quad (9)$$

As can be seen from (9), the output current i_{f2} lags the input voltage v_{ac} by 90° . Therefore, the voltage v_o in Fig. 3, which is defined as the voltage at the input side of the rectifier also lags v_{ac} by 90° . Due to the symmetry of the double-sided LCC

compensation network, L_{f2} resonates with C_{f2} while L_1 and C_1 are combined to resonate with C_{f1}

$$\omega L_{f2} - \frac{1}{\omega C_{f2}} = 0 \quad (10)$$

$$\omega L_1 - \frac{1}{\omega C_1} - \frac{1}{\omega C_{f1}} = 0. \quad (11)$$

By substituting (6), (7), (10), and (11) into the impedance equations, the secondary-side impedance Z_{sec} , the reflected impedance Z_{refl} , and the input impedance Z_{in} can be simplified as follows:

$$\begin{aligned} Z_{sec} &= j\omega L_2 + \frac{1}{j\omega C_2} + \frac{1}{j\omega C_{f2}} \parallel (j\omega L_{f2} + R_{eq}) \\ &= \frac{\omega^2 L_{f2}^2}{R_{eq}} \end{aligned} \quad (12)$$

$$Z_{refl} = \frac{-j\omega M i_2}{i_1} = \frac{\omega^2 M^2}{Z_{sec}}, \quad M = k\sqrt{L_1 L_2} \quad (13)$$

$$\begin{aligned} Z_{in} &= j\omega L_{f1} + \frac{1}{j\omega C_{f1}} \parallel \left(j\omega L_1 + \frac{1}{j\omega C_1} + Z_{refl} \right) \\ &= \frac{\omega^2 L_{f1}^2 L_{f2}^2}{M^2 R_{eq}} \end{aligned} \quad (14)$$

where M in (13) represents the mutual inductance between L_1 and L_2 . In this lossless analysis, the input power equals to the output power. Therefore, the expression of the system power is given by

$$\begin{aligned} P_{in} &= P_{out} = \left| \frac{V_{AC,RMS}}{Z_{in}} \right| \cdot V_{AC,RMS} \\ &= \frac{8k\sqrt{L_1 L_2} V_{in} V_{out}}{\pi^2 \omega L_{f1} L_{f2}}. \end{aligned} \quad (15)$$

The voltage at the input side of the rectifier v_o , the input current i_{f1} , and the current in the secondary main coil i_2 can be written as

$$v_o = i_{f2} \cdot R_{eq} = \frac{2\sqrt{2}}{\pi} V_{out} \angle -90^\circ \quad (16)$$

$$i_{f1} = -\frac{k\sqrt{L_1 L_2} v_o}{j\omega L_{f1} L_{f2}} = \frac{2\sqrt{2}}{\pi} \cdot \frac{k\sqrt{L_1 L_2} V_{out}}{j\omega L_{f1} L_{f2}} \angle 0^\circ \quad (17)$$

$$i_2 = -\frac{v_o}{j\omega L_{f2}} = \frac{2\sqrt{2}}{\pi} \cdot \frac{V_{out}}{\omega L_{f2}} \angle 0^\circ. \quad (18)$$

From (3), (9), (16), and (17), it is obvious that v_{ac} is in phase with i_{f1} and v_o is in phase with i_{f2} . Zero phase angle is achieved and no reactive power is needed from the power source. Moreover, v_{ac} leads v_o by 90° and the energy resonates between the primary side and secondary side back and forth.

III. DESIGN PROCEDURES

A. Main Coil Simulation

Based on (15), the coupling coefficient k between the main coils L_1 and L_2 is closely related to the power transfer ability of a WPT system with the double-sided LCC

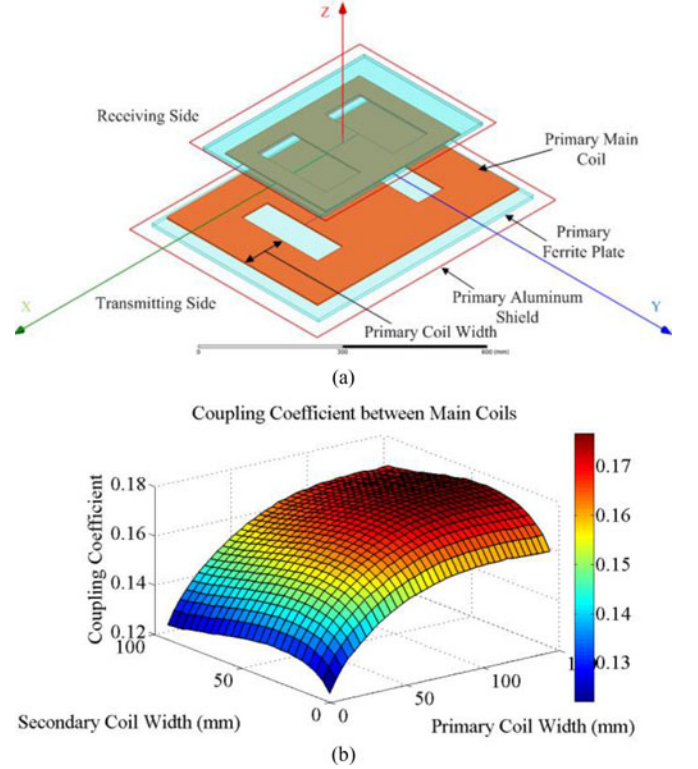


Fig. 4. (a) Overview of the main coil structure and (b) coupling coefficient k with different coil widths.

compensation topology. The value of k depends on the coil geometry. Therefore, once the dimensions of the coils are fixed, it is preferred to maximize k by changing the coil widths in both the primary and the secondary sides. Since the application is for passenger EVs, the space is quite limited on the vehicle. So, the receiving coil installed on the car is better to be smaller than the transmitting coil placed on the ground. Fig. 4(a) shows the overview of the proposed main coil structure. We decide to choose the dimension of the transmitting coil at the primary side as “600 mm * 450 mm * 4 mm” and that of the receiving coil at the secondary side as “400 mm * 300 mm * 4 mm.” Ferrite plates and aluminum shields are used for magnetic and electric shielding. They are also made successively larger to provide the needed shielding effects. The primary side ferrite plate has a dimension of “640 mm * 496 mm * 8 mm” while the secondary is “480 mm * 352 mm * 8 mm.” Aluminum shields are modeled with a primary dimension of “711.2 mm * 558.8 mm * 2 mm” and a secondary dimension of “508 mm * 406 mm * 2 mm.” As shown in Fig. 4(a), there are two design variables: the primary coil width and the secondary coil width. By varying the two variables, the coupling coefficient k can be maximized. In our case, k_{max} is 0.1764 with the primary coil width of 112 mm and the secondary coil width of 48 mm. Fig. 4(b) shows the simulation results.

B. Main Coil Winding and Measurement

Two design requirements must be met: 1) the designed resonant frequency is 85 kHz; and 2) the maximum efficiency is

achieved at the desired output power. Additionally, there are eight components in the double-sided compensation topology. If each component has a little variance from the designed value, it will be hard to meet the two requirements at the same time. Therefore, it is highly recommended to build and measure each component right after simulation.

C. Optimization of L_{f1} and L_{f2} at Maximum Efficiency

According to (15), once the resonant frequency, the system power, the main coupling coefficient, and the inductance values of the main coils are determined, the product of the compensated coil inductance values is fixed. A number of combinations could contribute to the same product and it is desired to optimize the values based on the efficiency curve of the system. The system is required to achieve the highest efficiency at the desired output power and the compensated inductance values can be optimized at that point. Once the output power is fixed, the system efficiency is determined by the power loss, which is closely related to the equivalent series resistance (ESR) of each component. The ESRs of the inductors can be calculated by their quality factors and inductance values and the ESRs of the capacitors rest with their dissipation factors. We can write expressions for the ESRs as

$$\begin{aligned} R_1 &= \frac{\omega L_1}{Q_1}, R_2 = \frac{\omega L_2}{Q_2}, R_{f1} = \frac{\omega L_{f1}}{Q_{f1}}, R_{f2} \\ &= \frac{\omega L_{f2}}{Q_{f2}} \end{aligned} \quad (19)$$

$$R_{C1} = DF \cdot \left| \frac{1}{j\omega C_1} \right|, R_{C2} = DF \cdot \left| \frac{1}{j\omega C_2} \right|$$

$$R_{Cf1} = DF \cdot \left| \frac{1}{j\omega C_{f1}} \right|, R_{Cf2} = DF \cdot \left| \frac{1}{j\omega C_{f2}} \right| \quad (20)$$

where Q_1 , Q_2 , Q_{f1} , and Q_{f2} stand for the quality factors of L_1 , L_2 , L_{f1} , and L_{f2} respectively. Q_1 and Q_2 can be measured by LCR meters since they have already been built in the last step. Q_{f1} and Q_{f2} can be approximated at 200 based on their inductance values, which are multiple times smaller than the main coil inductance values. DF is the dissipation factor of the capacitors. Once the compensated inductance values are given, the capacitance values can be calculated by (6), (7), (10), and (11). In this paper, 5PT series polypropylene and foil resonant power supply capacitors from Electronic Concepts are used and its DF is claimed to be 0.05%.

Fig. 5(a) and (b) shows the circuit diagram with ESRs added into the system. The system is divided into primary side circuit and the secondary side circuit. Therefore, the efficiency analysis can be done separately. The overall efficiency is the product of primary-side circuit efficiency η_{pri} and secondary-side efficiency η_{sec} . On the secondary side, η_{sec} is the product of η_{s1} , η_{s2} , and η_{s3} . As shown in Fig. 5(a), η_{s1} refers to efficiency of block 1, which is the ratio of the real power obtained by the load over the real power entering into block 1; η_{s2} is defined as the efficiency of block 2, which is the ratio of the real power entering into block 1 over the real power absorbed by block 2; η_{s3} is efficiency of block 3, which is the ratio of the real power

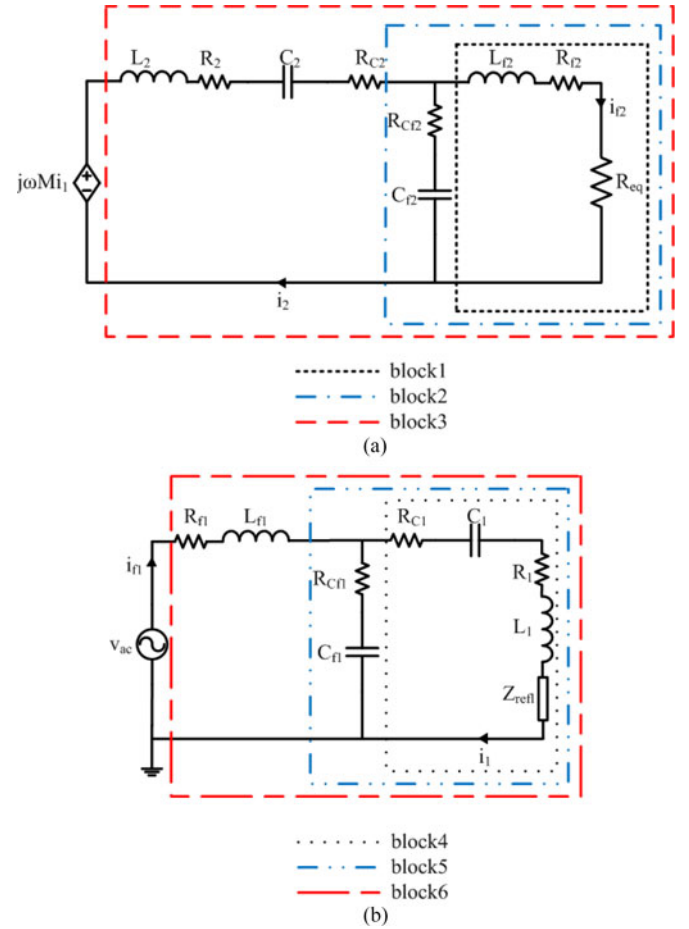


Fig. 5. Circuit diagrams with ESRs: (a) secondary side and (b) primary side.

absorbed by block 2 over the real power transferred from the primary side of the circuit. The expressions of η_{s1} , η_{s2} , and η_{s3} are given by

$$\begin{aligned} \eta_{s1} &= \frac{R_{eq}}{R_{eq} + R_{f2}}, \eta_{s2} = \\ &= \frac{|R_{Cf2} + \frac{1}{j\omega C_{f2}}|^2 \cdot (R_{eq} + R_{f2})}{|R_{Cf2} + \frac{1}{j\omega C_{f2}}|^2 \cdot (R_{eq} + R_{f2}) + |R_{eq} + R_{f2} + j\omega L_{f2}|^2 \cdot R_{Cf2}} \\ \eta_{s3} &= \frac{\text{Re}(Z_{block2})}{\text{Re}(Z_{block2}) + R_2 + R_{C2}} \end{aligned} \quad (21)$$

where Z_{block2} and Z_{sec} are the impedances of block 2 and the secondary-side circuit. Similarly, on the primary side, η_{pri} equals to the product of η_{p1} , η_{p2} , and η_{p3} . In Fig. 5 (b), η_{p1} is efficiency of block 4 and is given by the ratio of the real power transferred to the secondary side circuit over the real power going through block 4; η_{p2} is the efficiency of block 5 and expressed as the ratio of the real power going through block 4 over the real power received by block 5; η_{p3} is the efficiency of block 6 and described as the ratio of the real power received by block 5 over the real power sent by the power source. We derive expressions of η_{p1} , η_{p2} , and η_{p3} as (22) shown at bottom of the next page where Z_{refl} is the reflected impedance from the

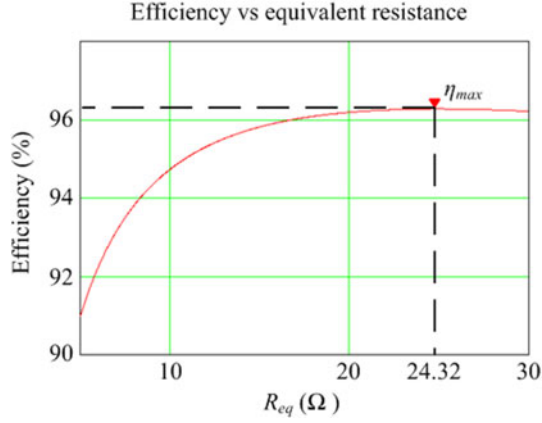


Fig. 6. Efficiency over equivalent resistance curve.

secondary-side circuit and Z_{block5} is the impedance of block 5. We can plot the efficiency over equivalent resistance curve by applying (21) and (22) in Mathcad. By adjusting the inductance values of L_{f1} and L_{f2} , the efficiency can be maximized at the desired equivalent resistance. For our case, the desired output power is 3.0 kW and the battery pack is 300 V; therefore, the efficiency is maximized at 24.32 Ω . Fig. 6 shows the efficiency curve obtained from Mathcad and the desired inductance values are determined as $L_{f1} = 46 \mu\text{H}$ and $L_{f2} = 38 \mu\text{H}$.

D. Maxwell Simulation for L_{f1} and L_{f2}

As analyzed in the previous section, a unipolar compensated coil is preferred in a coil structure with bipolar main coils. In order to further decrease the coupling effects between the main coil and the compensated coil, it is more desired to place the compensated coil in the region with weaker magnetic field densities. By substituting L_{f1} and L_{f2} into (8) and (18), the currents flowing through L_1 and L_2 can be determined and set as the excitation currents in the Maxwell model. Vacuum boxes are built up at the expected positions of the compensated coils, which are shown in Fig. 7(a). Fig. 7(b) shows the simulation results of magnetic flux densities in the vacuum boxes.

Clearly, the magnetic field is weaker in the central areas of the two main coils, which are circled by the dashed lines in Fig. 7(b). The compensated coils should be placed in those areas. With the desired inductance values, the compensated coils are built and simulated in ANSYS MAXWELL.

The compensated coils with the desired values are placed in the system as shown in Fig. 8(a) and the coupling coefficient k_{f1f2} is 0.05, which is good enough for the experiment. However, it can be further optimized. Since Fig. 7(b) indicates a larger

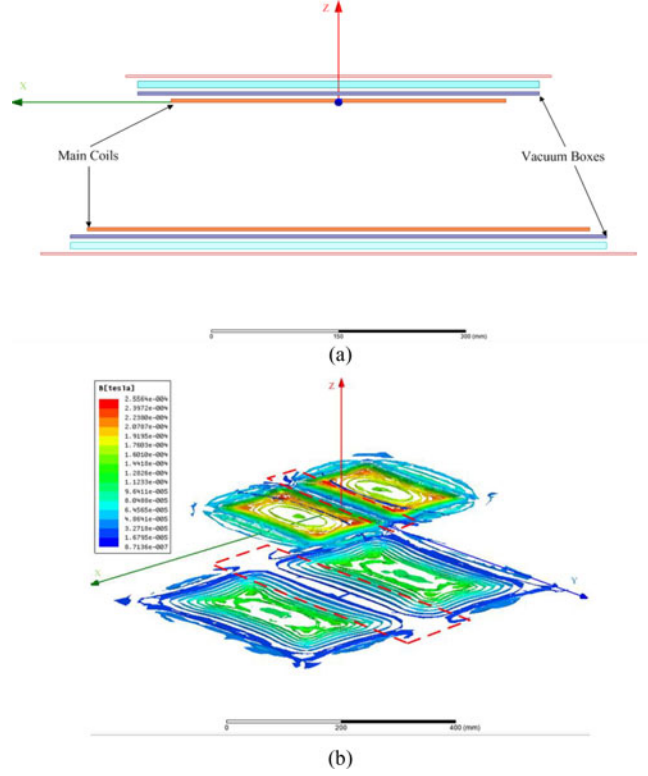


Fig. 7. (a) Side view of the coil structure with vacuum boxes and (b) magnetic field densities of the vacuum boxes.

area with weaker magnetic flux density on the primary side, so the primary compensated coil has enough area to be placed. By rotating the primary compensated coil from 0° to 180° as shown in Fig. 8(b), the lowest coupling case is achieved.

Fig. 9(a) shows the coupling coefficient k_{f1f2} of the compensated coils and the same-side coupling coefficients k_{1f1} and k_{2f2} . It is obvious that k_{f1f2} is minimized as 0.04 at 90° rotating angle while the same-side coupling coefficients are almost equal to zero with the angle rotating. Fig. 9(b) demonstrates that the self-inductance values of the two compensated coils keep almost constant with the angle rotating.

E. Compensated Coil Winding and Measurement

With the parameters provided by MAXWELL simulation, compensated coils are wound and measured. Again, in order to make the resonate frequency at 85 kHz and the efficiency maximized at the desired output power, capacitance values need to be recalculated with the measured results of L_1 , L_2 , L_{f1} , and L_{f2} through (6), (7), (10), and (11). The capacitance values

$$\eta_{p1} = \frac{\text{Re}(Z_{\text{refl}})}{\text{Re}(Z_{\text{refl}}) + R_{C1} + R_1}, \quad \eta_{p2} = \frac{\left| R_{Cf1} + \frac{1}{j\omega C_{f1}} \right|^2 \cdot [R_{C1} + R_1 + \text{Re}(Z_{\text{refl}})]}{\left| R_{Cf1} + \frac{1}{j\omega C_{f1}} \right|^2 \cdot [R_{C1} + R_1 + \text{Re}(Z_{\text{refl}})] + \left| R_1 + R_{C1} + j\omega L_1 + \frac{1}{j\omega C_1} + Z_{\text{refl}} \right|^2 \cdot R_{Cf1}}$$

$$\eta_{p3} = \frac{\text{Re}(Z_{\text{block5}})}{\text{Re}(Z_{\text{block5}}) + R_{f1}} \quad (22)$$

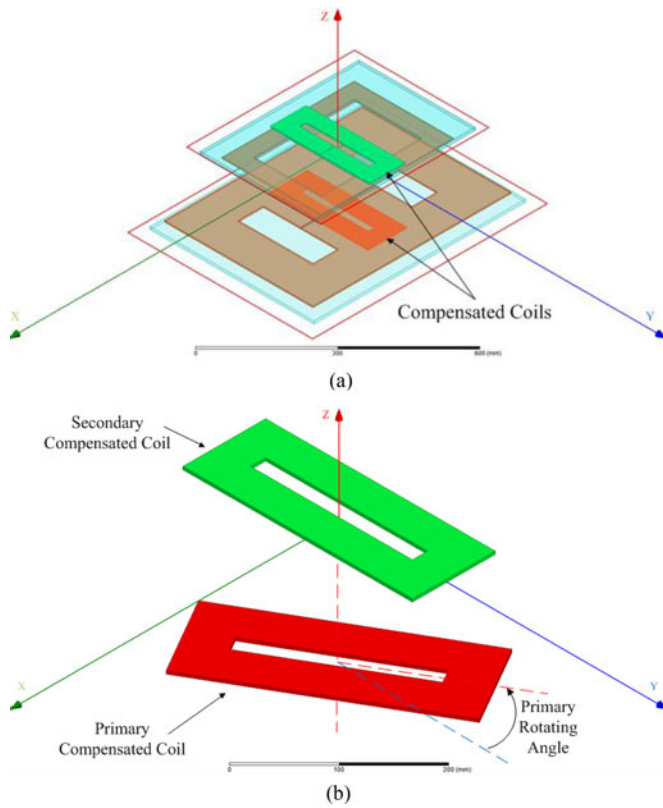


Fig. 8. (a) Coil structure with compensated coil integrated into the system and (b) rotating the primary compensated coil.

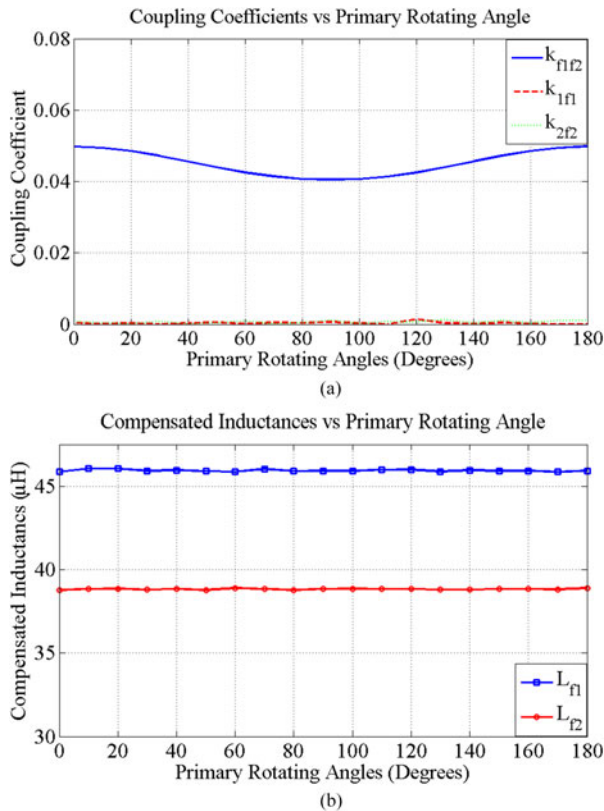


Fig. 9. (a) Coupling coefficients with rotating angles and (b) compensated inductance values with rotating angles.

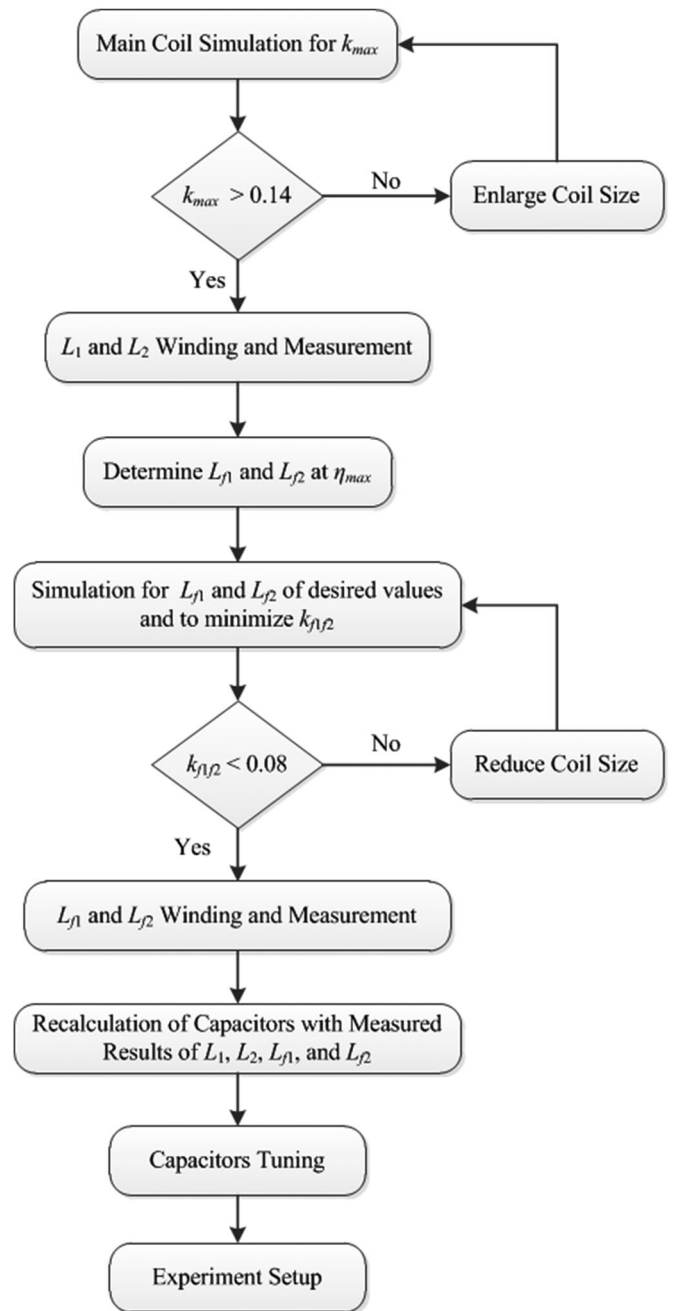


Fig. 10. Design flowchart.

calculated in this step only slightly vary from those calculated in step 3. Therefore, the efficiency will not be affected.

F. Capacitor Tuning for Zero Voltage Switching (ZVS)

ZVS not only reduces the switching noise of the MOSFETs, but also helps minimize the switching losses. In this paper, zero voltage turning on of the MOSFETs is achieved. We define the instantaneous current value when MOSFETs S_1 and S_4 are turned off as I_{OFF} . I_{OFF} must

$$I_{OFF} > \frac{2C_{OSS}V_{in,max}}{t_{dead}} \quad (23)$$

TABLE I
SYSTEM SPECIFICATIONS

Spec/Parameters	Design value
Input voltage	330 V
Battery pack voltage	300 V
Primary main coil dimension	600 mm × 450 mm × 4 mm
Secondary main coil dimension	400 mm × 300 mm × 4 mm
Primary ferrite plate dimension	640 mm × 496 mm × 8 mm
Secondary ferrite plate dimension	480 mm × 352 mm × 8 mm
Primary shield dimension	711 mm × 559 mm × 2 mm
Primary shield dimension	508 mm × 406 mm × 2 mm
Air gap	150 mm
Main coupling coefficient	0.1877
Resonant frequency	85 kHz
Maximum output power	3.0 kW

so that the current value is large enough to charge the parasitic output capacitors of S_1 and S_4 and discharge the parasitic output capacitors of S_2 and S_3 [14]. In (23), C_{oss} is the parasitic output capacitance of the MOSFET, $V_{in,max}$ is the maximum value of the input voltage, and t_{dead} is the dead time. In this paper, 1200 V C2M0025120D silicon carbide (SiC) Power MOSFETs from CREE are used. Its output parasitic capacitance is approximately 400 pF, $V_{in,max}$ is 330 V, and t_{dead} is 200 ns. Therefore, I_{OFF} should be larger than 1.32 A. During the dead time, the body diodes of the MOSFETs clamp the voltages over the parasitic output capacitors. Therefore, the parasitic output capacitors of S_1 and S_4 are charged to input voltage value and the parasitic output capacitors of S_2 and S_3 are discharged to almost 0 V. So, when S_2 and S_3 are turned on right after the dead time, the voltages across them are almost zero and zero voltage turning on of S_2 and S_3 is achieved. Similarly, zero voltage turning on of S_1 and S_4 is achieved after half a cycle. Based on [14], the capacitor C_2 is the best choice to tune in order to achieve ZVS. It is demonstrated that C_2 is tuned to be 8–11% larger than the calculated value of C_2 in the last step. Once the previous six steps are done, it is ready to build the wireless charging system and conduct experiments. The design procedures can be summarized in the flowchart as shown in Fig. 10. In particular, the two design criterions of k_{max} and k_{f1f2} are the authors' experienced values, which are the worst cases to make the system work as well.

IV. EXPERIMENT

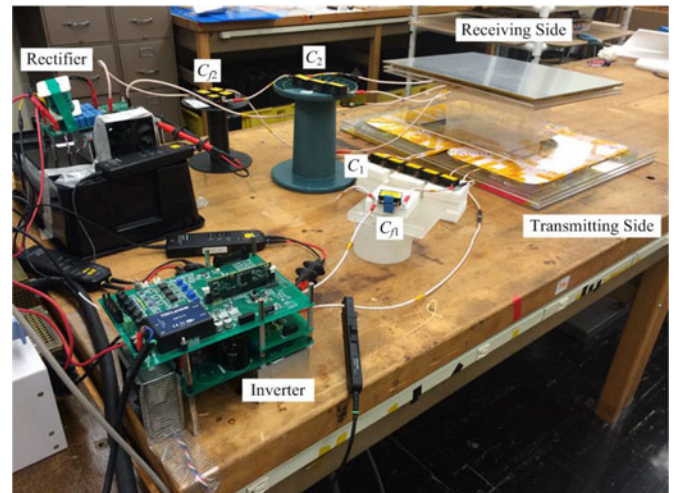
The system specifications are given in Table I. Since the resonant frequency is fixed at 85 kHz, AWG-38 copper wires are selected to minimize the skin effect. The input voltage is 330 V, the output battery pack voltage is 300 V, and the output power is 3.0 kW. Therefore, 800-strand AWG-38 litz wires are used. The ferrite is Ferroxcube 3C95, which has outstanding performance at frequencies below 500 kHz. Aluminum plates serve as the electric shielding. The air gap is 150 mm due to the ground clearance of passenger cars. Based on simulations results, the main coils are built and compensated coils are integrated, which are shown in Fig. 11(a) and (b). Fig. 11(c) presents the whole wireless charging system. It shows that it is highly compact with the compensated coil integrated into the system. The circuit



(a)



(b)



(c)

Fig. 11. Experiment setup of (a) coils on primary side, (b) coils on secondary side, and (c) wireless charging system.

parameters are given in Table II. It is convinced that there are only slight differences between the design values and the measured values.

Table III compares the simulated results and measured results of the six coupling coefficients in the wireless charging system. Clearly, the measured results prove that not only are the same-side coupling coefficients k_{1f1} and k_{2f2} eliminated, but also the cross-side coupling coefficients k_{1f2} and k_{2f1} , the coupling coefficient of compensated coil k_{f1f2} are minimized to negligible levels. The maximum main coupling coefficient

TABLE II
CIRCUIT PARAMETERS

Parameters	Design value	Measured value
Primary main coil inductance L_1	225.35 μH	222.98 μH
Secondary main coil inductance L_2	159.45 μH	157.55 μH
Primary compensated coil inductance L_{f1}	46 μH	44.059 μH
Secondary compensated coil inductance L_{f2}	38 μH	38.04 μH
Primary resonant capacitor C_1	19.59 nF	19.853 nF
Secondary resonant capacitor C_2	31.39 nF	32.71 nF
Primary compensated capacitor C_{f1}	79.68 nF	79.69 nF
Secondary compensated capacitor C_{f2}	92.16 nF	92.36 nF

TABLE III
COUPLING COEFFICIENTS

Coupling coefficients	Simulated value	Measured value
Main coupling coefficient k	0.1746	0.1877
Coupling coefficient k_{1f1} between L_1 and L_{f1}	0.00068	0.005826
Coupling coefficient k_{2f2} between L_2 and L_{f2}	0.001118	0.012368
Coupling coefficient k_{1f2} between L_1 and L_{f2}	≈ 0	0.006135
Coupling coefficient k_{2f1} between L_2 and L_{f1}	≈ 0	0.002941
Coupling coefficient k_{f1f2} between L_{f1} and L_{f2}	0.04053	0.0483

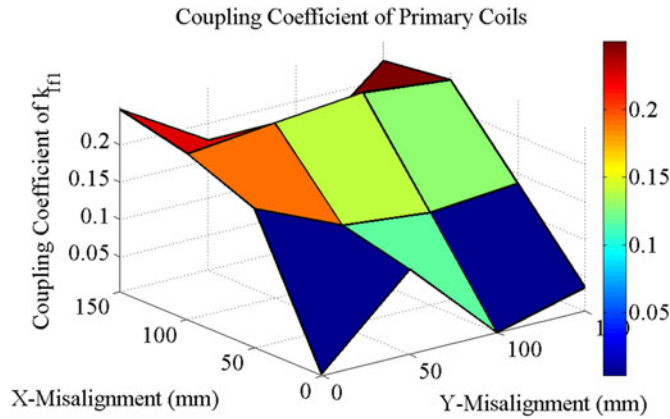


Fig. 12. Horizontal misalignment effects on k_{1f1} .

k is achieved at 0.1877. The measured results of k and k_{f1f2} match their simulated results since they are relatively large when compared to k_{1f1} , k_{2f2} , k_{1f2} , and k_{2f1} . The percentages of the errors between the simulated results and the measured results for k_{1f1} , k_{2f2} , k_{1f2} , and k_{2f1} are large. It is because their values are very small and only a slight misalignment will result in a big difference in results. Fig. 12 further demonstrates that the center of the compensated coil should be aligned with the center of the main coil so that the same-side coupling coefficient is eliminated. Fig. 13 shows how the measured coupling coefficients k_{f1f2} , k_{1f1} , and k_{2f2} vary with the compensated coils rotating. As shown in Fig. 13(a), k_{f1f2} is minimized when the primary rotating angle equals 90° and secondary rotating angle is 0° , which verifies the simulation result in Fig. 9(a). The measured results in Fig. 13(b) and (c) indicate that k_{1f1} and k_{2f2} are small enough to be neglected, further confirming the proposed idea. Fig. 14 presents the measured results of the two compensated coils. The inductance values keep constant at the

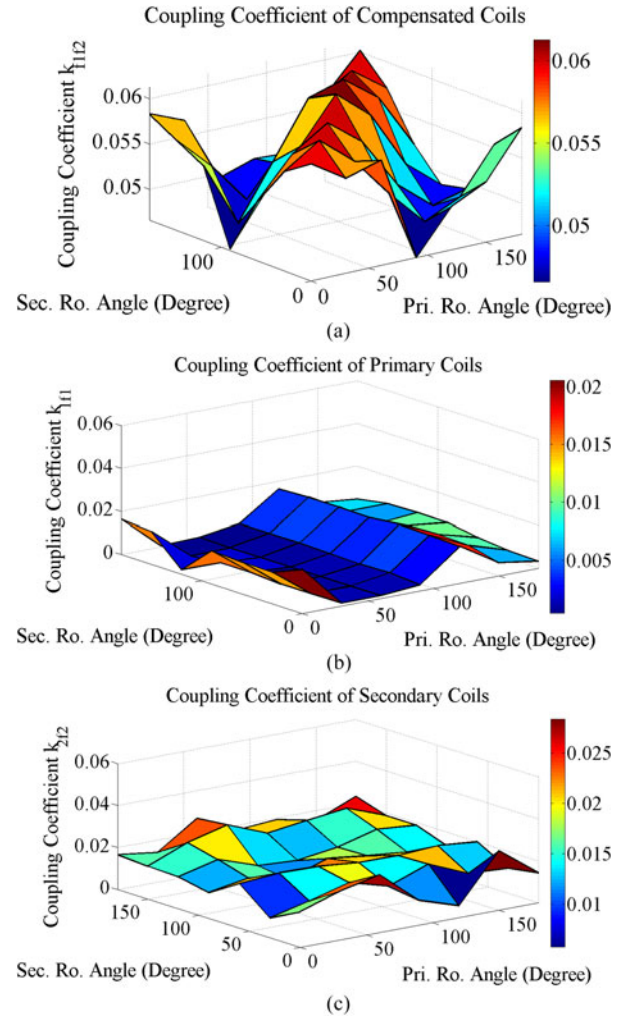


Fig. 13. Coupling coefficients (a) k_{f1f2} , (b) k_{1f1} , and (c) k_{2f2} with compensated coils rotating.

designed values with the angles rotating, which also confirms the simulation results in Fig. 9(b).

Fig. 15(a) represents the waveforms of the primary resonant tank's input voltage v_{ac} and input current i_{f1} , the secondary resonant tank's output voltage v_o , and MOSFET gate-to-source voltage V_{drive} . In this paper, the purpose of observing V_{drive} is to ensure that the gate-to-source voltage is in its maximum rating all the time since noises may appear during the experiment. Here, v_{ac} leads i_{f1} by 13.4° and the turn-off current I_{OFF} is approximately 4.5 A, which is much larger than 1.32 A and sufficient for charging and discharging the parasitic output capacitors. Fig. 15(b) shows power characteristics of the wireless charging system at the maximum output power. When fully aligned, the system is able to deliver 3.0 kW output power at dc-dc efficiency as high as 95.5%. Further experiments on misalignments are also conducted in the Y-direction, X-direction, and Z-direction separately. Fig. 16(a)–(c) shows the respective waveforms. Since the input voltage and the battery pack voltage are fixed at 330 and 300 V, the waveforms of v_{ac} and v_o remain the same. However, the waveform of i_{f1} gradually deviates from its original waveform shown in Fig. 15(a). When misalignments

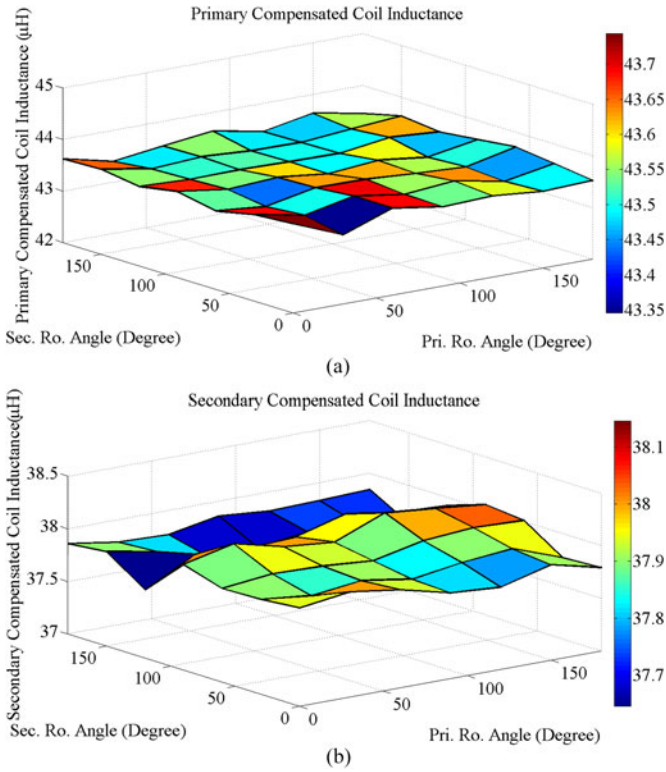


Fig. 14. Compensated inductances values (a) L_{f1} and (b) L_{f2} with the compensated coils rotating.

in different directions occur, the main coupling coefficient k decreases and the output power goes down, as indicated by (15). Therefore, the rms value of i_{f1} becomes smaller. Moreover, the mutual inductance M between the main coils decreases and as a result, both the reflected impedance Z_{refl} and input impedance Z_{in} change. The input phase angle between v_{ac} and i_{f1} increases, which causes the turn-off current I_{OFF} to increase and the high-order harmonics components in i_{f1} to rise. The decreased rms value of i_{f1} , the increased turn-off current value and high-order harmonics components in i_{f1} result in the waveform distortions when misalignments occur. Fig. 16(a) shows the waveforms when Y-direction misalignment is 150 mm. Since k and M are still comparable to their original values when fully aligned, the waveform distortion of i_{f1} is low. However, when k and M further decreases, the waveform distortion turns high, as shown in Fig. 16(b) and (c). Here, Z-direction misalignment is 50 mm means air gap is increased from 150 to 200 mm.

All the experimental results are given by Fig. 17. The solid line in Fig. 17 (a) shows the experimental result when the system is fully aligned. It shows great consistency with the simulated efficiency curve in Fig. 6 and the system efficiency is peaked at the maximum output power. The dash-dot line presents the result of the experiment on Z-direction misalignment. The system can transfer 1.76 kW at efficiency of 94.4% when the air gap increases to 200 mm. The solid line with circles gives the system performance on X-direction misalignment. The system delivers 1.57 kW power at an efficiency of 93.8% when the X-direction misalignment increases to 100 mm. The performance is a little weaker and as a result, it is highly recommended to make X-

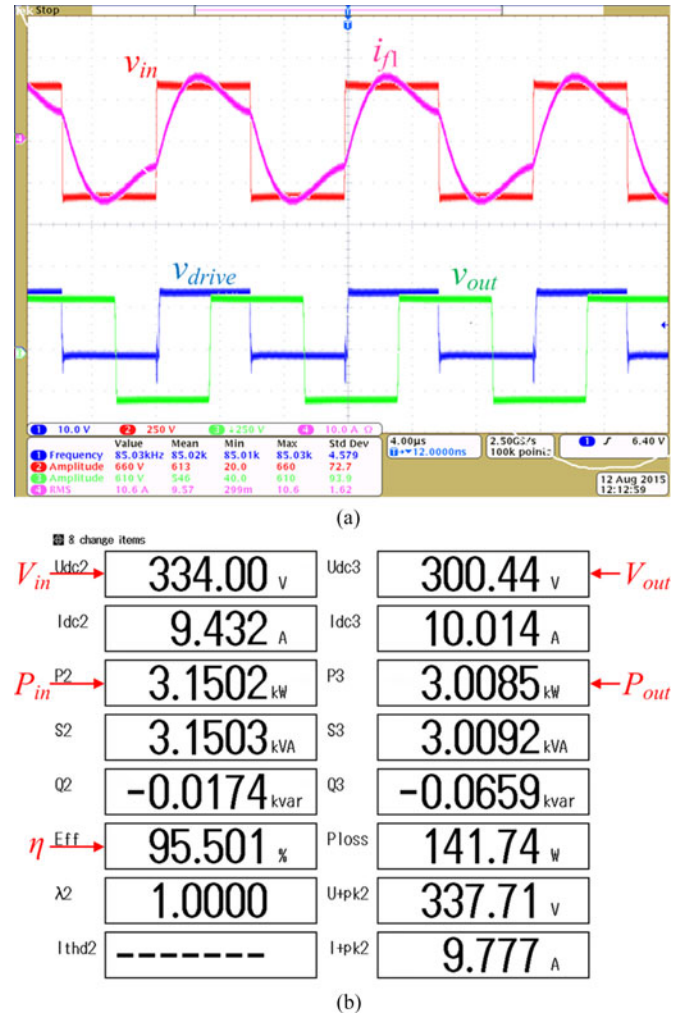


Fig. 15. (a) Waveforms when fully aligned and (b) system power characteristics with $V_{in} = 334$ V, $V_{out} = 300$ V, $P_{in} = 3.15$ kW, $P_{out} = 3.01$ kW, and $\eta = 95.5\%$.

direction compliant with the front-rear direction of the car since it is more convenient for the driver to adjust when the car is parked. The dashed and dotted lines show the system performance in Y-direction. The system performs much better in this direction. When the misalignment even increases to 150 mm, the system can still deliver approximately 2.0 kW at an efficiency of 94.8%. This direction is better to be door-to-door direction since it is hard for drivers to adjust when the car is parked. Fig. 17(a) indicates that when misalignment in different directions occurs, the output power drops 33.33% from the maximum output power in Y-direction, 41.33% in Z-direction, and 47.69% in X-direction. It is because the main coupling coefficient k decreases and other component values remain almost the same, as it is indicated by (15). Fig. 17(b) shows how the measured main coupling coefficient k decreases as misalignment occurs. When the misalignment increases to 150 mm in Y-direction, k decreases to 0.1244, or 33.72% drop from its original value ($k = 0.1877$); when the misalignment increases to 50 mm in Z-direction, k goes down to 0.1045, or 44.33% drop; when the misalignment increases to 100 mm in X-direction, k declines to

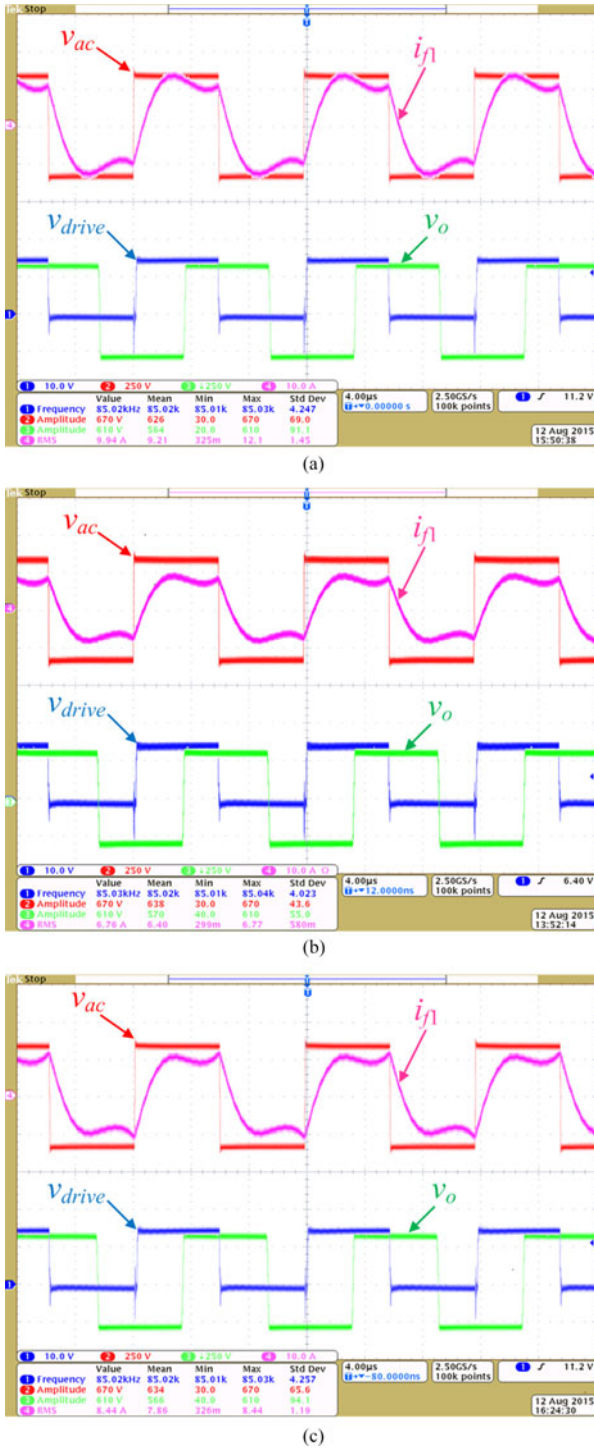


Fig. 16. Waveforms when misalignments in different directions occur: (a) Y-direction misalignment is 150 mm, (b) Z-direction misalignment is 50 mm, and (c) X-direction misalignment is 100 mm.

0.1, or 46.72% drop. The differences in the respective dropped percentages between the output power and the main coupling coefficient are caused by the differences in inductance values when misalignment occurs. However, the differences are within 3%, indicating the inductance values only slightly change. Fig. 17(a) and (b) not only verify (15), but also validate that extra coupling coefficients are eliminated or minimized to a negligible level.

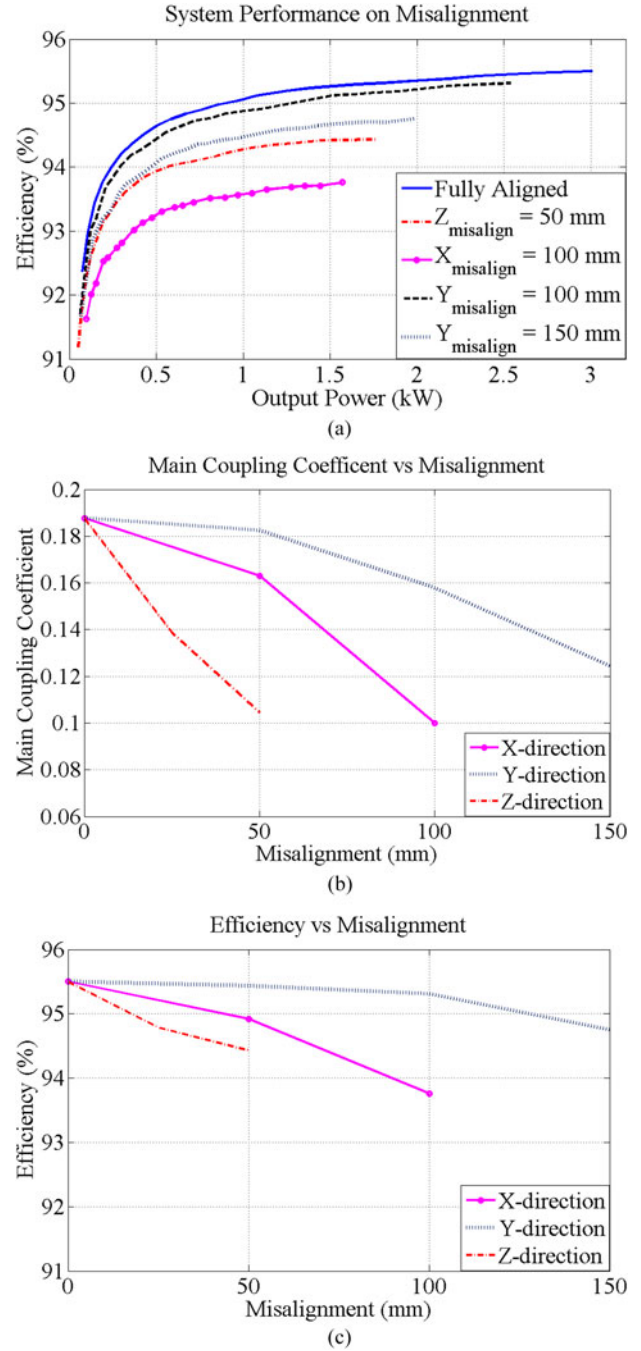


Fig. 17. Experimental results on misalignments in different directions: (a) efficiency versus output power, (b) main coupling coefficient versus misalignment, and (c) efficiency versus misalignment.

Fig. 17(c) describes how the efficiency varies with misalignments in different directions. It turns out that the efficiency decreases as the misalignment increases. Furthermore, the efficiency curve in Fig. 17(c) shows fairly good consistency with the main coupling coefficient curve in Fig. 17(b). Experimental results demonstrate the wireless charging system with the new integration method not only has the dual advantage of compactness and high efficiency, but also eliminates the extra coupling effects or minimize them to a negligible level, which greatly simplifies the system analysis and design.

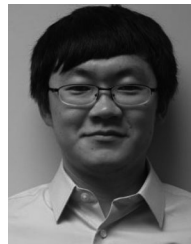
V. CONCLUSION

This paper gives a new integrated method of a wireless charging system using double-sided LCC compensation topology. With the compensated coils integrated into the main coil structure, the system becomes much more compact. The proposed compensated coil design further eliminate or minimize the extra coupling effects to a negligible level, making it more straightforward to design a wireless charging system using the double-sided LCC compensation topology. The detailed design procedures to improve system efficiency are also introduced. Both the 3-D FEA simulation results and the experimental results verify the proposed idea. The compact and highly efficient wireless charging system is able to deliver 3.0 kW at a dc–dc efficiency of 95.5% with an air gap of 150 mm when fully aligned.

Our future work is to install the designed wireless charger on a vehicle. In order to achieve that, we will not only analyze the additional power loss resulted from ambient objects, such as the EV chassis and the steels buried in the ground, but also optimize the ferrite plates so that minimum ferrite bars are employed to deliver the same amount of power with competitive efficiency.

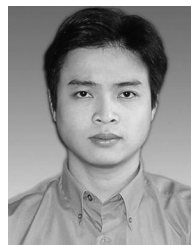
REFERENCES

- [1] J. H. Hertz, *Dictionary of Scientific Biography*. New York, NY, USA: Scribner, vol. VI, 1970, pp. 340–349.
- [2] N. Tesla, “Apparatus for transmitting electrical energy,” U.S. Patent 1 119 732, Dec. 1914.
- [3] W. C. Brown, “The history of power transmission by radio waves,” *IEEE Trans. Microw. Theory Tech.*, vol. MTT-32, no. 9, pp. 1230–1242, Sep. 1964.
- [4] J. Garnica, R. A. Chinga, and J. Lin, “Wireless power transmission: From far field to near field,” *Proc. IEEE*, vol. 101, no. 6, pp. 1321–1331, Apr. 2013.
- [5] A. Kurs, A. Karalis, R. Moffatt, J. D. Joannopoulos, P. Fisher, and M. Soljacic, “Wireless power transfer via strongly coupled magnetic resonances,” *Science*, vol. 317, no. 5834, pp. 83–86, Jul. 2007.
- [6] R. Wu, W. Li, H. Luo, J. K. O. Sin, and C. P. Yue, “Design and characterization of wireless power links for brain-machine interface applications,” *IEEE Trans. Power Electron.*, vol. 29, no. 10, pp. 5462–5471, Jan. 2014.
- [7] D. Ahn and P.P. Mercier, “Wireless power transfer with concurrent 200 kHz and 6.78 MHz operation in a single transmitter device,” *IEEE Trans. Power Electron.*, vol. 31, no. 7, pp. 5018–5029, Jul. 2016.
- [8] M. Budhia, G. A. Covic, and J. T. Boys, “Design and optimization of circular magnetic structures for lumped inductive power transfer systems,” *IEEE Trans. Power Electron.*, vol. 26, no. 11, pp. 3096–3018, Apr. 2011.
- [9] H. Takanashi, Y. Sato, Y. Kaneko, S. Abe, and T. Yasuda, “A large air gap 3 kW wireless power transfer system for electric vehicles,” in *Proc. IEEE Energy Convers. Congr. Expo.*, 2012, pp. 269–274.
- [10] M. Budhia, J. T. Boys, G. A. Covic, and C. Huang, “Development of a single-sided flux magnetic coupler for electric vehicle IPT charging systems,” *IEEE Trans. Ind. Electron.*, vol. 60, no. 1, pp. 318–328, Sep. 2011.
- [11] T. Nguyen, S. Li, W. Li, and C.C. Mi, “Feasibility study on bipolar pads for efficient wireless power chargers,” in *Proc. IEEE Appl. Power Electron. Conf. Expo.*, 2014, pp. 1676–1682.
- [12] Z. Pantic, S. Bai, and S. Lukic, “ZCS LCC-compensated resonant inverter for inductive-power-transfer application,” *IEEE Trans. Ind. Electron.*, vol. 58, no. 8, pp. 3500–3510, Sep. 2010.
- [13] S. Li, W. Li, J. Deng, T. D. Nguyen, and C. C. Mi, “A double-sided LCC compensation network and its tuning method for wireless power transfer,” *IEEE Trans. Veh. Technol.*, vol. 64, no. 6, pp. 2261–2273, Aug. 2014.
- [14] W. Li, H. Zhao, S. Li, J. Deng, T. Kan, and C. C. Mi, “Integrated LCC compensation topology for wireless charger in electric and plug-in electric vehicles,” *IEEE Trans. Ind. Electron.*, vol. 62, no. 7, pp. 4215–4225, Dec. 2014.
- [15] J. Deng, W. Li, T. D. Nguyen, S. Li, and C. C. Mi, “Compact and efficient bipolar coupler for wireless power chargers: Design and analysis,” *IEEE Trans. Power Electron.*, vol. 30, no. 11, pp. 6130–6140, Mar. 2015.
- [16] J. Deng, W. Li, S. Li, and C. C. Mi, “Magnetic integration of LCC compensated resonant converter for inductive power transfer applications,” in *Proc. IEEE Energy Convers. Congr. Expo.*, 2014, pp. 660–667.
- [17] R. L. Steigerwald, “A comparison of half-bridge resonant converter topologies,” *IEEE Trans. Power Electron.*, vol. 3, no. 2, pp. 174–182, Apr. 1998.
- [18] A. Peverè, R. Petrella, C. C. Mi, and S. Zhou, “Design of a high efficiency 22 kW wireless power transfer system for EVs fast contactless charging stations,” in *Proc. IEEE Electr. Veh. Conf.*, 2014, pp. 1–7.
- [19] J. Lee and B. Han, “A bidirectional wireless power transfer EV charger using self-resonant PWM,” *IEEE Trans. Power Electron.*, vol. 30, no. 4, pp. 1784–1787, Apr. 2015.
- [20] C. Park, S. Lee, G. Cho, and C. T. Rim, “Innovative 5-m-off-distance inductive power transfer systems with optimally shaped dipole coils,” *IEEE Trans. Power Electron.*, vol. 30, no. 2, pp. 817–827, Mar. 2014.
- [21] F. Lu, H. Zhang, H. Hofmann, and C. C. Mi, “A high efficiency 3.3 kW loosely-coupled wireless power transfer system without magnetic material,” in *Proc. IEEE Energy Convers. Congr. Expo.*, 2015, pp. 2282–2286.
- [22] A. Kamineni, G. A. Covic, and J. T. Boys, “Analysis of coplanar intermediate coil structures in inductive power transfer systems,” *IEEE Trans. Power Electron.*, vol. 30, no. 11, pp. 6141–6154, Nov. 2015.
- [23] W. Zhang and C. C. Mi, “Compensation topologies for high power wireless power transfer systems,” *IEEE Trans. Veh. Technol.*, vol. PP, no. 99, pp. 1–10, Jul. 2015, DOI:10.1109/TVT.2015.2454292.



Tianze Kan (S'15) received the B.Eng. degree in electrical engineering and automation from the Huazhong University of Science and Technology, Wuhan, China, in 2011, and the M.S. degree in electrical engineering from the University of Southern California, Los Angeles, CA, USA, in 2013. He is currently working toward the Ph.D. degree in electrical and computer engineering in the joint doctoral program between San Diego State University and the University of California at San Diego, La Jolla, CA, USA.

His research interests include inductive-based wireless power transfer, especially on coil design and compensation topologies.



Trong-Duy Nguyen was born in Binh Dinh, Vietnam. He received the B.Eng. and M.Eng. degrees from the Hochiminh-City University of Technology, Hồ Chí Minh, Vietnam, in 2004 and 2007, respectively, and the Ph.D. degree from the Nanyang Technological University, Singapore, Singapore, in 2012.

His current research interests include electrical machine design and drives, electromagnetics, and electrical energy conversion systems.



Jeff C. White received the Associates degree in motive power technology from St Clair College, Windsor, ON, Canada, in 1981.

His first R&D position was with CNG Systems in Livonia, MI, USA, for development of compressed natural gas dual fuel systems for light vehicles in 1986, and he was a Supervisor with AMC/Chrysler Aero Dynamics laboratories in 1988. While at DENSO International America, Inc., since 1988, he was responsible for management of vehicle and component testing of fuel systems, thermal systems, and NVH areas. His major achievements were Denso to GM, Ford, Chrysler wind tunnel correlation and ISO QS 9000 Lead Auditor. As a Senior Manager, he became responsible for of all testing facilities including overseeing testing facility designs and implementation including ISO 17025 Laboratory Accreditation and GM, Ford, Chrysler AEMCLRP certification for Emissions Radiated and Conducted Testing. His key initial research areas were alternative fuels with focus on NH₃ from wind power. He is currently overseeing collaborative academic projects related to vehicle electrification such as, in wheel motors and wireless charging. His keen interests are simulation modeling to experimental validations as related to human safety.



Rajesh K. Malhan (M'11) received the M.Sc. (electronics), M.Phil., and Ph.D. degrees from the University of Delhi, New Delhi, India, in 1982, 1984, and 1989, respectively.

He was a Postdoctoral Research Fellow in the Department of Electrical and Electronic Engineering (Electron Device Group), Toyohashi University of Technology, Japan, till March 1991. He joined DENSO Corporation (formerly Nippondenso Co., Ltd.) same year, where he was responsible for III-V compound semiconductor electrical and optical device R&D at DENSO headquarter, Kariya. In 1996, he started working in DENSO Research Laboratories, where he played the major role in established a major research program in the field of wide band gap semiconductor silicon carbide power electronics (power device and modules). He is the Director of advanced research at DENSO's North American Research and Development Department. He is responsible for DENSO's Automotive (Autonomous drive, Vehicle electrification, Vehicle wireless charging, Alternative fuel and Metal air battery technologies) R&D work. He has published more than 50 research journal papers, inventor or coinventor on more than 25 US and 150 international patents, and contributed chapters in four books.

Dr. Malhan is a winner of 24th Japan Society of Applied Physics year 2002 award for outstanding achievements in the field of applied physics. He is a member of the Society of Automotive Engineers (USA), the Japan Society of Applied Physics (Japan), and served on many international professional society committees.



Chunting Chris Mi (S'00-A'01-M'01-SM'03-F'12) received the B.S.E.E. and M.S.E.E. degrees in electrical engineering from Northwestern Polytechnical University, Xi'an, China, in 1985 and 1988, respectively, and the Ph.D. degree in electrical engineering from the University of Toronto, Toronto, ON, Canada, in 2001.

He is a Professor and Chair of electrical and computer engineering and the Director of the Department of Energy-funded Graduate Automotive Technology Education Center for Electric Drive Transportation, San Diego State University, San Diego, CA, USA. Prior to joining SDSU, he was with the University of Michigan, Dearborn, from 2001 to 2015. He was the President and the Chief Technical Officer of 1Power Solutions, Inc., from 2008 to 2011. He is the Co-Founder of Gannon Motors and Controls LLC and Mia Motors, Inc. He has conducted extensive research and has published more than 100 journal papers. He has taught tutorials and seminars on the subject of HEVs/PHEVs for the Society of Automotive Engineers, the IEEE, workshops sponsored by the National Science Foundation, and the National Society of Professional Engineers. He has delivered courses to major automotive OEMs and suppliers, including GM, Ford, Chrysler, Honda, Hyundai, Tyco Electronics, A&D Technology, Johnson Controls, Quantum Technology, Delphi, and the European Ph.D. School. He has offered tutorials in many countries, including the U.S., China, Korea, Singapore, Italy, France, and Mexico. He has published more than 100 articles and delivered 30 invited talks and keynote speeches. He has also served as a Panelist in major IEEE and SAE conferences. His research interests include electric drives, power electronics, electric machines, renewable-energy systems, and electrical and hybrid vehicles.

Dr. Mi is the recipient of "Distinguished Teaching Award" and "Distinguished Research Award" of University of Michigan Dearborn. He is a recipient of the 2007 IEEE Region 4 "Outstanding Engineer Award," "IEEE Southeastern Michigan Section Outstanding Professional Award," and the "SAE Environmental Excellence in Transportation."